

Amine-assisted synthesis of FeS@N-C porous nanowires for highly reversible lithium storage

Xiujuan Wei[§], Xin Tan[§], Jiasheng Meng, Xuanpeng Wang, Ping Hu, Wei Yang, Shuangshuang Tan, Qinyou An (✉), and Liqiang Mai (✉)

State Key Laboratory of Advanced Technology for Materials Synthesis and Processing, Wuhan University of Technology, Wuhan 430070, China

[§] Xiujuan Wei and Xin Tan contributed equally to this work.

Received: 8 April 2018

Revised: 30 May 2018

Accepted: 30 June 2018

© Tsinghua University Press and Springer-Verlag GmbH Germany, part of Springer Nature 2018

KEYWORDS

iron sulfide,
N-doped carbon matrix,
porous nanowires,
lithium-ion batteries,
superior cycling stability

ABSTRACT

Iron sulfide is an attractive anode material for lithium-ion batteries (LIBs) due to its high specific capacity, environmental benignity, and abundant resources. However, its application is hindered by poor cyclability and rate performance, caused by a large volume variation and low conductivity. Herein, iron sulfide porous nanowires confined in an N-doped carbon matrix (FeS@N-C nanowires) are fabricated through a simple amine-assisted solvothermal reaction and subsequent calcination strategy. The as-obtained FeS@N-C nanowires, as an LIB anode, exhibit ultrahigh reversible capacity, superior rate capability, and long-term cycling performance. In particular, a high specific capacity of 1,061 mAh·g⁻¹ can be achieved at 1 A·g⁻¹ after 500 cycles. Most impressively, it exhibits a high specific capacity of 433 mAh·g⁻¹ even at 5 A·g⁻¹. The superior electrochemical performance is ascribed to the synergistic effect of the porous nanowire structure and the conductive N-doped carbon matrix. These results demonstrate that the synergistic strategy of combining porous nanowires with an N-doped carbon matrix holds great potential for energy storage.

1 Introduction

Rechargeable lithium-ion batteries (LIBs) have been widely applied in portable electronic devices and have also been developed for use in electric vehicles and large-scale energy storage devices owing to their high energy density and environmental benignity [1–3]. To meet the increasing requirement of these emerging large-scale energy storage applications, it is

highly desired to develop high-performance LIBs based on advanced anode materials. Graphite, as a commercial LIB anode material, delivers a low theoretical specific capacity of 372 mAh·g⁻¹ and a limited rate property [4, 5]. Among anode materials, transition-metal chalcogenides (TMCs) are regarded as potential candidates, owing to their high capacity, cost effectiveness, environmental benignity, and enhanced safety [6–10]. However, TMC electrodes

Address correspondence to Liqiang Mai, mlq518@whut.edu.cn; Qinyou An, anqinyou86@whut.edu.cn

suffer from a large volume variation during the Li⁺ insertion/extraction process, leading to rapid capacity fading and a loss of electrical conductivity.

Structural and compositional engineering has been employed to solve these problems of TMCs [11–15]. Decreasing the dimensions of TMCs to a nanometer range can shorten the ion diffusion pathway and thereby enhance the electrochemical property of electrode materials. Designing nanowires with a porous structure is also an effective strategy to enhance the cycling stability. In such nanostructures, nanowires provide short ion diffusion distances, while the void space can alleviate the structural strain during the lithiation/delithiation processes [16–20]. In addition, confining the electrode materials to conductive carbonaceous networks can enhance the electrical conductivity of the electrode materials, prevent their pulverization, and buffer their volume change, leading to a high lithium storage performance [21–28]. As a result, considerable efforts have been applied based on the above strategies. For example, Hu et al. reported a template-induced formation of CoSe@carbon nanoboxes with advantageous nanoarchitectures [29]. The CoSe@carbon nanoboxes show high specific capacity, excellent rate performance, and superior cyclability. Wang et al. synthesized a unique one-dimensional anatase TiO₂ modified FeS nanostructure, displaying superior lithium storage performance with high capacity, excellent cyclic stability, and enhanced rate property, compared with those of pure FeS nanostructures [30]. Yang et al. synthesized hierarchical MoS₂/PANI nanowires from MoO_x-based organic-inorganic hybrids, exhibiting greatly improved lithium ion storage performance due to the hierarchical textures and the PANI-hybrid structures [31]. Thus, integrating the advantages of one-dimensional porous nanostructures and a conductive carbon matrix is desirable for high-performance TMC anode materials. As a typical metal sulfide, FeS has drawn extensive attention owing to its high theoretical capacity, low cost, and abundant resources. To the best of our knowledge, iron sulfide porous nanowires confined in an N-doped carbon matrix have rarely been reported due to the difficulties of synthetic chemistry.

In this work, we have constructed iron sulfide porous nanowires confined in an N-doped carbon

matrix (FeS@N-C nanowires) by a facile amine-assisted solvothermal reaction and subsequent calcination strategy. When tested as an LIB anode, the as-prepared FeS@N-C nanowires manifest ultrahigh reversible capacity, superior rate capability, and long-term cycling performance. In addition, the lithium-storage mechanism has been systematically investigated via *ex-situ* X-ray diffraction (XRD) and high-resolution transmission electron microscopy (HRTEM).

2 Experimental

2.1 Material synthesis

Synthesis of FeS@N-C nanowires: FeSO₄·7H₂O (1 mmol) was dispersed into distilled H₂O (25 mL). Then, thioacetamide (TAA, 2 mmol) was added into the above solution. Thereafter, ethylene glycol (5 mL) and ethylenediamine (5 mL) were added into the mixed solution. Finally, the as-prepared solution was transferred into a Teflon-lined stainless steel autoclave. The autoclave was kept at 180 °C for 24 h. The precipitate obtained from the autoclave was washed with deionized water and ethanol several times and dried at 70 °C for 12 h. The obtained precursors were calcinated at 500 °C with a rate of 1 °C·min⁻¹ for 2 h under H₂/Ar atmosphere. For comparison, FeS@N-C microsheets were fabricated by the same procedure with ethylenediamine (15 mL) and a total solution volume of 35 mL; a caved FeS polyhedron was synthesized by the same procedure without ethylenediamine and the calcination process.

2.2 Characterization

X-ray diffraction (XRD) patterns were recorded using a D8 Discover X-ray diffractometer with Cu K α radiation. The carbon content was measured using a Vario EL cube CHNSO elemental analyzer. Field-emission scanning electron microscopy (FESEM) images were collected using a JEOL-7100F microscope. Transmission electron microscopy (TEM) images and the corresponding element mapping analyses were collected using a JSM-2010 microscope. X-ray photoelectron spectroscopy (XPS) analysis was carried out on a VG 110 Multilab 2000. AFM images were obtained using a SmartSPMTM-1000 scanning probe

microscope.

2.3 Electrochemical measurements

The electrochemical performances were investigated by assembling 2016-type coin cells in a glove box. The working electrodes consisted of the obtained active materials, acetylene black, and carboxymethyl cellulose (CMC), with a weight ratio of 70:20:10. The separator used was a Celgard 2300 membrane. The electrolyte was a solution of 1 M LiPF₆ in ethylene carbonate (EC), dimethyl carbonate (DMC), and methyl carbonate (EMC) (1:1:1, vol.%). Galvanostatic charge/discharge measurements were conducted using a multichannel battery testing system (LAND CT2001A). Cyclic voltammetry (CV) and electrochemical impedance spectroscopy (EIS) were performed using electrochemical workstations (CHI600D and Autolab Potentiostat Galvanostat 302N). These measurements were carried out at room temperature.

3 Results and discussion

3.1 Structural characterization

In the constructed structure, composite nanowires with abundant voids can not only shorten the ion diffusion distance and offer a continuous electron transport pathway, but also relieve the volume expansion during the Li⁺ insertion/extraction process. Moreover, the N-doped carbon matrix can improve the electrical conductivity of the electrode and reinforce its structural integrity (Fig. 1(a)). The schematic diagrams of the synthesis processes of the FeS@N-C nanowires, FeS@N-C microsheets, and caved FeS polyhedron are displayed in Fig. 1(b) and Figs. S1 and S2 in the Electronic Supplementary Material (ESM), respectively. These three samples with different morphologies are prepared by changing the amount of ethylenediamine added. The ethylenediamine molecules are protonated and formed positively charged ammonium ions under the solvothermal conditions. The protonated ethylenediamine molecules act as structure-directing agents, which can induce the anisotropic growth of 1D nanostructures and the formation of 1D inorganic–organic hybrids [32–34]. As the reaction and dispersion medium, ethylene

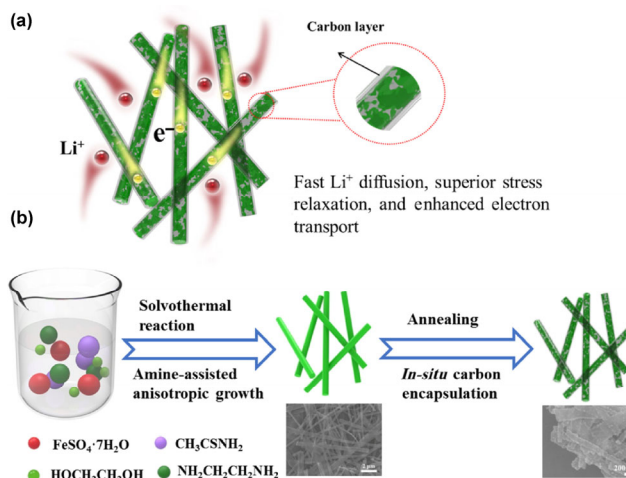


Figure 1 (a) Schematic illustration of the porous FeS@N-C nanowires with fast Li⁺ diffusion, superior stress relaxation, and enhanced electron transport during Li⁺ extraction/insertion. (b) Schematic representation of the fabrication process of porous FeS@N-C nanowires.

glycol can effectively adsorb onto the surface of the particles, which is beneficial for the production of monodispersed metal sulfides with good dispersivity [35, 36]. The scanning electron microscopy (SEM) images of the as-prepared FeS@N-C nanowire precursor are shown in Fig. S3 in the ESM. It can be observed that the obtained precursors have a uniform nanowire structure. The Fourier transform infrared spectroscopy (FT-IR) and XPS spectra of the as-prepared FeS@N-C nanowire precursors are also characterized. The FT-IR result shows that the vibration bands of –CH₂–, –NH₂, and C–N suggest the existence of ethylenediamine in the precursors (Fig. S4 in the ESM) [37]. In addition, the XPS spectrum shows that the binding energies of N 1s are identified at 399.4 and 401.3 eV, corresponding to the non-protonated and protonated amine, respectively (Fig. S5 in the ESM) [38]. During the calcination process, ethylenediamine also acts as the carbon and nitrogen source, confining the growth of FeS. It is noted that the amount of ethylenediamine has a great influence on the final morphology. On increasing the amount of ethylenediamine, the presence of more template molecules induces the formation of the microsheet structure (Fig. S6 in the ESM).

The XRD patterns of the as-prepared FeS@N-C nanowires, caved FeS polyhedron, and FeS@N-C microsheets are depicted in Fig. 2(a) and Figs. S7(a) and S7(b) in the ESM, respectively. The XRD peaks

can be indexed to the monoclinic FeS phase (JCPDS card No. 00-017-0200) free of impurities. The morphologies of the FeS@N-C nanowires are characterized using SEM and TEM. It is observed that the as-prepared sample has a uniform structure of nanowires with widths of 200–500 nm and lengths up to several micrometers (Fig. 2(b) and Fig. S8 in the ESM). The high-magnification TEM image displayed in Fig. 2(c) shows the as-prepared FeS@N-C nanowires with a porous structure containing numerous nanovoids. The nanovoids are randomly distributed in the obtained nanowires. A d -spacing of 2.62 Å is observed in Fig. 2(d), corresponding to the (404) plane of the FeS crystal. The high-angle annular dark-field (HAADF) and corresponding elemental mapping images shown in Figs. 2(e)–2(i) indicate the coexistence and homogeneous dispersion of the elements Fe, S, C, and N in the as-prepared sample. Moreover, the carbon matrix is uniformly coated on the surface of the nanowires.

Figures S7(c)–S7(f) in the ESM show the SEM images of the as-prepared caved FeS polyhedron and FeS@N-C microsheets. The SEM images (Figs. S7(c) and S7(d) in the ESM) indicate that the caved polyhedron is assembled by the sheets and possesses a size of 4–5 μm . The thicknesses of the sheets are in

the range of 500–600 nm. The FeS@N-C microsheets exhibit sizes ranging from 2 to 4 μm (Figs. S7(e) and S7(f) in the ESM). The TEM and HAADF elemental mapping images (Fig. S9 in the ESM) indicate that some nanosheets are dispersed on the surface of the microsheets and the elements Fe, S, C, and N are uniformly distributed in the obtained product. The thicknesses of the nanowires and microsheets are confirmed by AFM measurements (Fig. S10 in the ESM). The thickness of the nanowires is about 11 nm (Figs. S10(a) and S10(b) in the ESM). It can be seen that the microsheets are stacks of multi-layer thin nanosheets and the thickness of a single-layer nanosheet is about 12 nm (Figs. S10(c) and S10(d) in the ESM). The CHNS analysis result (Table S1 in the ESM) shows that the carbon and nitrogen contents of the FeS@N-C nanowires are 2.83 wt.% and 1.91 wt.%, respectively; the carbon and nitrogen contents of the FeS@N-C microsheets are 5.08 wt.% and 3.56 wt.%, respectively.

The reaction time and temperature also play important roles in the formation of the FeS@N-C nanowire precursors. A series of control experiments were carried out. The precursors formed at 120 $^{\circ}\text{C}$ were fragments, and a very small number of nanowires existed, which may result from the low reaction kinetics

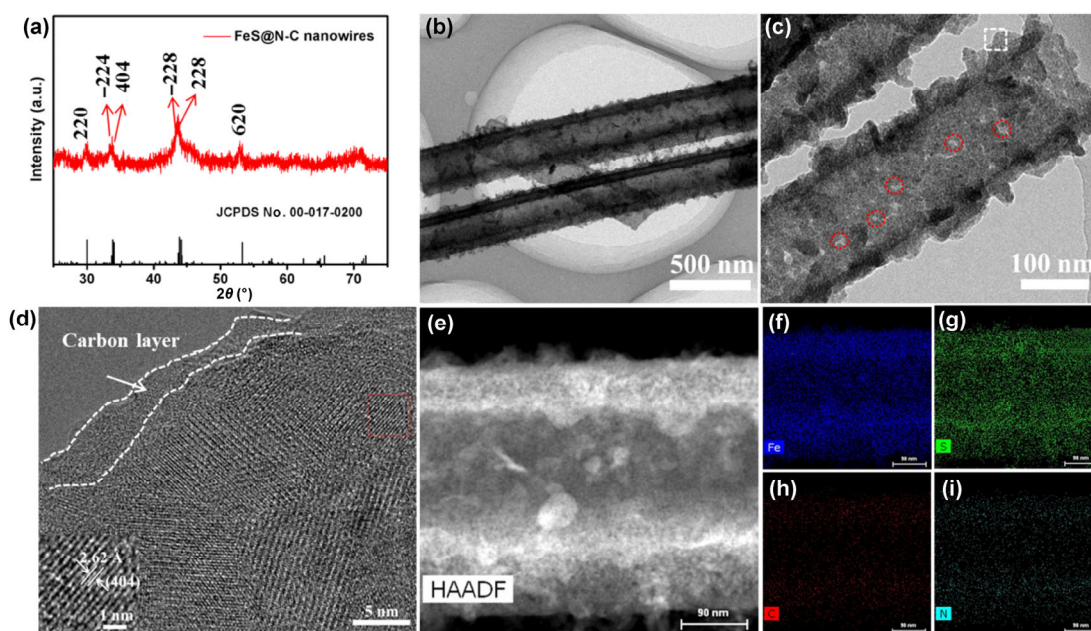


Figure 2 Structural characterizations of FeS@N-C nanowires. (a) XRD pattern of FeS@N-C nanowires. (b)–(d) Low-magnification, high-magnification, and high-resolution TEM images of FeS@N-C nanowires. (e)–(i) HAADF and corresponding elemental mapping images of FeS@N-C nanowires, the scale bars are 90 nm.

at the low temperature (Figs. S11(a) and S11(b) in the ESM). When the temperature increased to 160 °C, a large number of nanowires were generated (Figs. S11(c) and S11(d) in the ESM). However, the nanowires grew wider at a higher temperature of 200 °C (Figs. S11(e) and S11(f) in the ESM). This indicates that a suitable temperature is necessary for the formation of nanowires. When the reaction temperature is 180 °C, large sheets have been generated and some nanoribbons are torn from their surface after a reaction time of 6 h (Figs. S12(a) and S12(b) in the ESM). After the reaction time increased to 12 h, an increasing number of nanoribbons were torn from the surface of the sheets and finally transformed into nanowires (Figs. S12(c) and S12(d) in the ESM). Thus, the reaction time is an important factor for determining the shapes of the precursors. The influence of the annealing temperature on the formation of a nanovoid structure has also been studied. Figures S13(a)–S13(d) in the ESM show the SEM and TEM images of the FeS@N-C nanowires annealed at 600 °C. It can be observed that larger voids formed in the nanowires. This is analogous to the formation process of porous structures driven by the Kirkendall diffusion effect [39, 40]. However, with increased annealing temperature, the nanowire structure was damaged to a certain extent.

3.2 Electrochemical performance in LIBs

In order to verify the advantage of the unique FeS@N-C nanowire structure, the lithium-storage performances of the as-prepared FeS@N-C nanowires, FeS@N-C microsheets, and caved FeS polyhedron were investigated by assembling half-cells. The cycling performances of the obtained FeS@N-C nanowires, FeS@N-C microsheets, and caved FeS polyhedron at 0.2 A·g⁻¹ are displayed in Fig. 3(a). The as-prepared FeS@N-C nanowires deliver a higher discharge specific capacity and better cycling stability than those of the FeS@N-C microsheets and caved FeS polyhedron. The discharge capacity of the FeS@N-C nanowire electrode is 821 mAh·g⁻¹ during the 50th cycle, and reaches 987 mAh·g⁻¹ during the 100th cycle. However, the FeS@N-C microsheets and caved FeS polyhedron only deliver a discharge specific capacity of 617 and 432 mAh·g⁻¹, respectively, during the 50th cycle. The rate capabilities of the as-prepared FeS@N-C nanowires,

FeS@N-C microsheets, and caved FeS polyhedron were tested at various current densities ranging from 0.5 to 5 A·g⁻¹, as represented in Fig. 3(b). The average discharge capacities of the FeS@N-C nanowires are 979, 810, 662, 540, and 433 mAh·g⁻¹ at different current densities of 0.5, 1, 2, 3, and 5 A·g⁻¹, respectively. By contrast, the FeS@N-C microsheets and caved FeS polyhedron show comparable, low capacities at current densities ranging from 0.5 to 5 A·g⁻¹. These results confirm that the FeS@N-C nanowires have better rate and cycling properties than those of the FeS@N-C microsheets and caved FeS polyhedron. The long-term cycling stability of the FeS@N-C nanowires was examined at 1 A·g⁻¹ (Fig. 3(c)). They exhibit superior cycling performance, achieving a high reversible capacity of 1,061 mAh·g⁻¹ after 500 cycles. The phenomenon of the capacity increase beyond the theoretical capacity (609 mAh·g⁻¹) can also be observed in carbon-based metal oxide anode materials, and is attributed to the enhanced ion diffusion kinetics owing to the activation process and reaction between metal particles and electrolytes [21, 41]. Figure 3(d) shows the charge/discharge voltage profiles of the FeS@N-C nanowires at 1 A·g⁻¹ in the voltage range of 0.01–3 V. During the first discharge process, a large plateau at around 1.29 V and a broad plateau at 0.79 V can be observed. These are attributed to the multistep lithiation mechanism and the formation of a solid electrolyte interlayer [42, 43]. The as-prepared FeS@N-C nanowires exhibit excellent reversible cycling behavior. The rate capability of the FeS@N-C nanowires is compared with those of other reported FeS-based anodes for LIBs (Fig. 3(e)), including FeS@RGO composites [44], FeS@TiO₂ [30], FeS microsheets networks [45], G@FeS-GNR composites [46], C@FeS nanosheets [43], and FeS@C/Carbon cloth [47]. Clearly, the as-prepared FeS@N-C nanowires exhibit a higher capacity and better rate properties than those of the previously reported electrodes, showing a great promise for high-performance LIB application. To fully illustrate the advantages of the FeS@N-C nanowires, the EIS spectra of the as-prepared FeS@N-C nanowires, FeS@N-C microsheets, and caved FeS polyhedron were measured as shown in Fig. S14 in the ESM. The medium-frequency semicircle reveals the charge-transfer resistance (R_{ct}), and the low-frequency

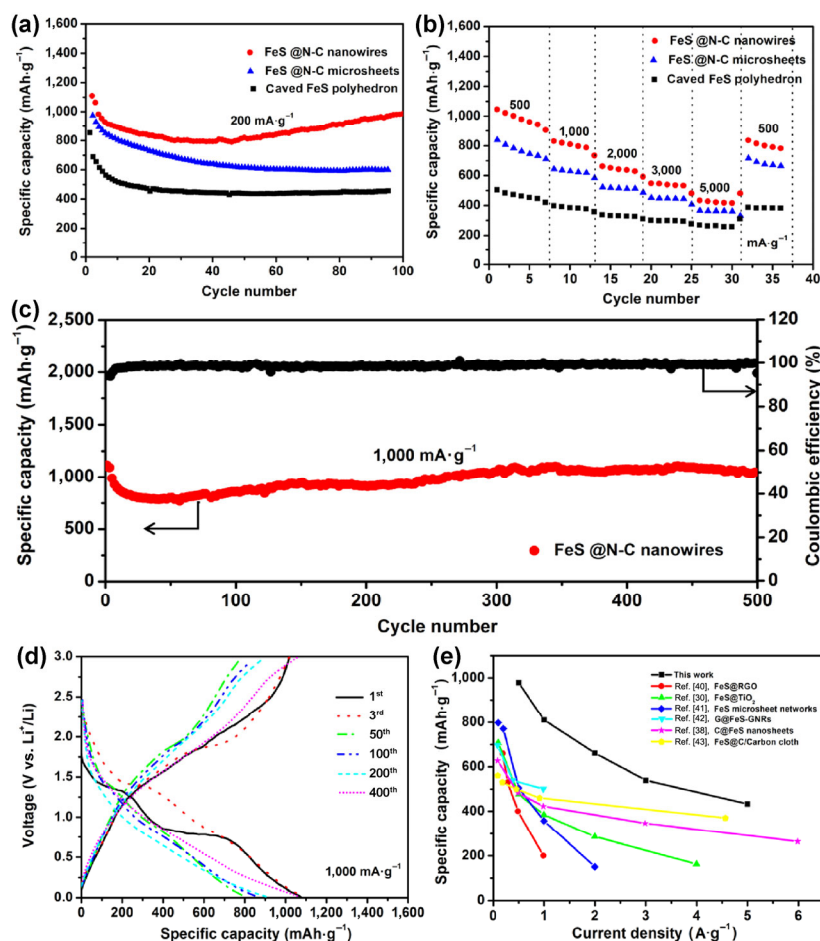


Figure 3 Electrochemical properties of FeS@N-C nanowires, FeS@N-C microsheets, and caved FeS polyhedron for lithium-ion storage. (a) Cycling performance at a current of 200 mA·g⁻¹. (b) Rate performance at current densities ranging from 0.5 to 5 A·g⁻¹. (c) Long-life cycling performance of FeS@N-C nanowires at 1,000 mA·g⁻¹. (d) Charge-discharge voltage profiles of FeS@N-C nanowire electrode in the potential range of 0.01–3.0 V (vs. Li⁺/Li) at 1,000 mA·g⁻¹ for the 1st, 3rd, 50th, 100th, 200th, and 400th cycles. (e) Comparison of rate capability of prepared FeS@N-C nanowires with those of other reports.

region represents the ion diffusion process [48]. It can be seen that the FeS@N-C nanowires show the smallest R_{ct} among the three samples, demonstrating faster electrochemical kinetics of the FeS@N-C nanowire electrode. The superior electrochemical performances of the FeS@N-C nanowires can be attributed to the one-dimensional porous nanowire structure, which shortens the ion diffusion distance and releases the mechanical strain. Meanwhile, the homogeneous N-doped carbon encapsulation not only enhances electron transport but also buffers the volume expansion of electrodes.

The CV curves for the as-prepared FeS@N-C nanowires, FeS@N-C microsheets, and caved FeS polyhedron were recorded at various scan rates from 0.2 to

1.0 mV·s⁻¹ (Figs. 4(a)–4(c)). It can be observed that two peaks exist in the initial cathodic sweep, which is in accordance with previous reports [9]. In the first cycle, the oxidation peak at around 1.9 V is attributed to the lithiation process from metal to metal sulfides [45, 49]. The CV curves of the FeS@N-C nanowires overlapped better than those of the FeS@N-C microsheets and caved FeS polyhedron, demonstrating the better cycling reversibility of the FeS@N-C nanowires. The lithium-diffusion coefficients of the three samples were confirmed based on the Randles–Sevcik equation [50, 51]

$$I_p = 0.4463nFAC(nFvD/RT)^{1/2} = [(269,000)n^{3/2}AD^{1/2}C]v^{1/2} \quad (1)$$

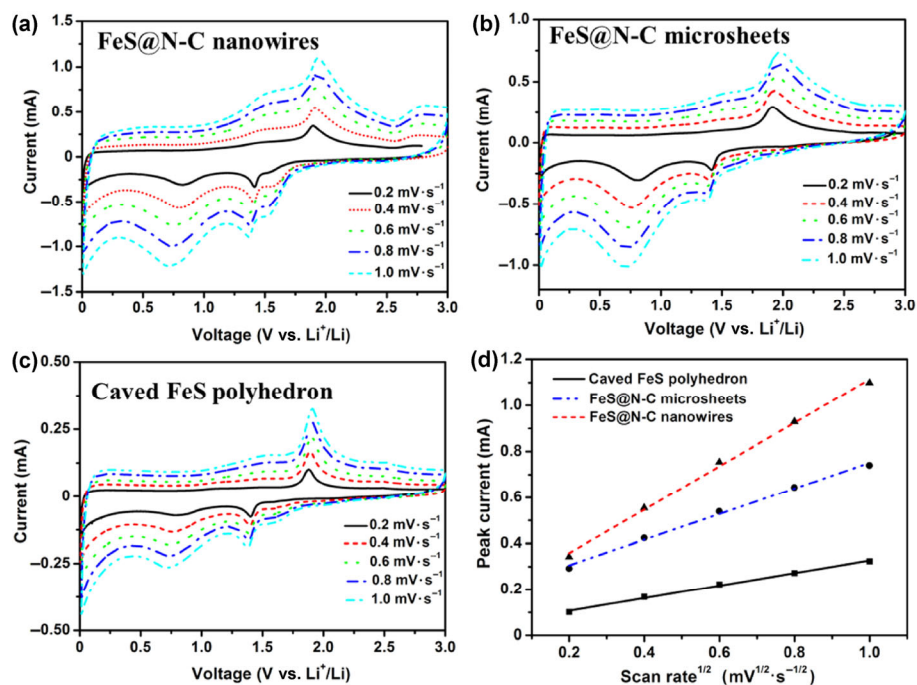


Figure 4 (a)–(c) CV curves of FeS@N-C nanowires, FeS@N-C microsheets, and caved FeS polyhedron at different scan rates, respectively. (d) Randles–Sevcik plots obtained from the CV data.

in which I_p is the peak current, D , n , A , F , C , and v represent the diffusion coefficient, the number of electrons transferred in the electrochemical reaction, the surface area of the electrodes, the Faraday constant, the concentration of ions, and the scan rate, respectively. The plots of I_p vs. $v^{1/2}$ shown in Fig. 4(d) were studied regarding the oxidation peak current at about 1.9 V. From Eq. (1), the calculated lithium diffusion coefficient of the FeS@N-C nanowires ($2.49 \times 10^{-6} \text{ cm}^2 \cdot \text{s}^{-1}$) is much higher than that of the FeS@N-C microsheets ($8.7 \times 10^{-7} \text{ cm}^2 \cdot \text{s}^{-1}$) and caved FeS polyhedron ($2.1 \times 10^{-7} \text{ cm}^2 \cdot \text{s}^{-1}$). The high ion diffusion coefficient is beneficial for the enhancement of the electrochemical performance of the electrode materials.

To study the electrochemical reaction mechanism and structural stability of the FeS@N-C nanowires, *ex-situ* XRD, SEM, and TEM were carried out. The *ex-situ* XRD patterns and corresponding high-resolution TEM images of the electrodes discharged to 0.01 V and charged to 3 V for the first cycle at $200 \text{ mA} \cdot \text{g}^{-1}$ are shown in Fig. 5(a). When the cell was discharged to 0.01 V, the phases Li_2FeS_2 and Li_2S can be detected in the XRD patterns, indicating that the intercalation and conversion reaction occurred in the FeS electrode.

d -spacings of 2.02 and 3.15 Å can be detected in the HRTEM image of the electrode discharged to 0.01 V (inset of Fig. 5(a)), and can be ascribed to the (220) planes of Li_2S (JCPDS card No. 01-077-2145) and (002) planes of Li_2FeS_2 (JCPDS card No. 01-080-0578), respectively. When the cell was charged to 3 V, the XRD patterns obtained can be assigned to the phases of iron sulfide. In addition, the S phase can also be detected, which indicates that S^{2-} is at least partially transformed into S^0 during the cycling process. This result is in good agreement with those of previous works [52, 53]. A d -spacing of 2.70 Å can be observed in the high-resolution TEM image of the electrode charged to 3 V (inset of Fig. 5(a)), corresponding to the (411) planes of FeS (JCPDS card No. 00-017-0200). The above results indicate that the lithium storage mechanism of the FeS electrode is based on the intercalation and conversion reactions. Figure 5(b) shows the SEM images of the FeS@N-C nanowires at the initial state, discharged to 0.01, and charged to 3 V. It is observed that the morphology of the FeS@N-C nanowires can be well-preserved after lithium ion insertion/extraction, which demonstrates that the unique nanowire structure can effectively relieve the

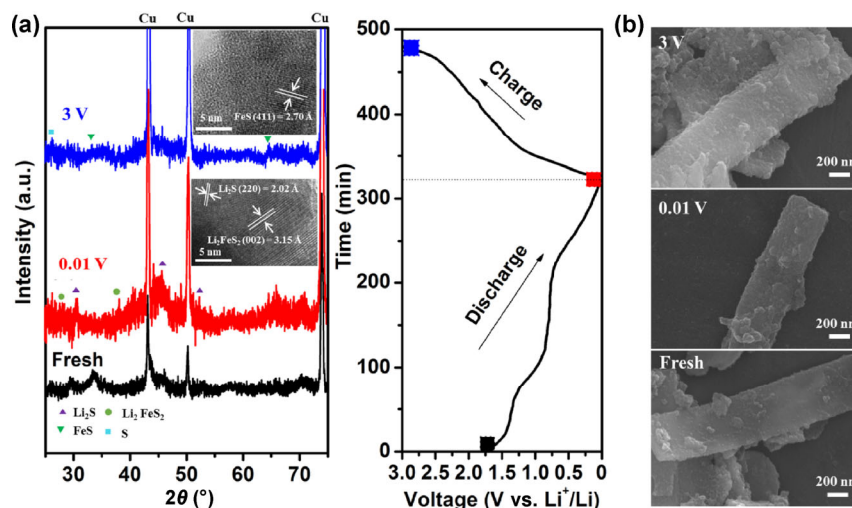


Figure 5 (a) *Ex-situ* XRD patterns and the corresponding high-resolution TEM images of FeS@N-C nanowires discharged to 0.01 V and charged to 3 V for the first cycle at $200 \text{ mA} \cdot \text{g}^{-1}$. (b) SEM images of FeS@N-C nanowires at initial state, discharged to 0.01 V, and charged to 3 V.

volume expansion of the electrode during the ion insertion/extraction process, and thereby enhance the cycling stability of electrodes.

4 Conclusions

In summary, a FeS@N-C nanowire architecture is successfully prepared through a facile amine-assisted solvothermal reaction and subsequent calcination process. When the FeS@N-C nanowires are assessed as an anode material for LIBs, they exhibit superior electrochemical performance, including high reversible capacity with excellent cycling stability ($1,061 \text{ mAh} \cdot \text{g}^{-1}$ after 500 cycles at $1 \text{ A} \cdot \text{g}^{-1}$) and high rate capability ($433 \text{ mAh} \cdot \text{g}^{-1}$ at $5 \text{ A} \cdot \text{g}^{-1}$). The excellent electrochemical performance of the FeS@N-C nanowires can be attributed to the short ionic diffusion distance, enhanced electrical conductivity, and better stress accommodation. The synergistic strategy of combining porous nanowires with an N-doped carbon matrix has great potential in solving the volume expansion and low conductivity issues of metal sulfide anode materials.

Acknowledgements

This work was supported by the National Key Research and Development Program of China (Nos. 2016YFA0202601 and 2016YFA0202603), the National

Natural Science Foundation of China (Nos. 51425204 and 51602239), the Hubei Provincial Natural Science Foundation of China (No. 2016CFB267), the Fundamental Research Funds for the Central Universities (No. 2017-CL-A1-43). Prof. Liqiang Mai gratefully acknowledged financial support from China Scholarship Council (No. 201606955096).

Electronic Supplementary Material: Supplementary material (schematic representation of the fabrication process of FeS@N-C microsheets and caved FeS polyhedron; SEM images, FT-IR spectrum and XPS spectrum of the N 1s region of the as-prepared FeS@N-C nanowire precursors; SEM images of the as-prepared FeS@N-C microsheets precursors; XRD patterns and SEM images of caved FeS polyhedron and FeS@N-C microsheets; SEM image of the as-prepared FeS@N-C nanowires; TEM images of the FeS@N-C microsheets; AFM images and surface topographies of FeS@N-C nanowires and microsheets on a silica surface; SEM images of the nanowire precursors prepared at 120, 160, 200 °C; SEM images of the nanowire precursors with different reaction durations: 6, 12 h; SEM and TEM images of the FeS@N-C nanowires annealed at 600 °C; EIS of FeS@N-C nanowires, FeS@N-C microsheets and caved FeS polyhedron before cycling; weight percent of C, N and S of FeS@N-C nanowires and FeS@N-C microsheets) is available in

the online version of this article at <https://doi.org/10.1007/s12274-018-2140-7>.

References

- [1] Ji, L. W.; Lin, Z.; Alcoutlabi, M.; Zhang, X. W. Recent developments in nanostructured anode materials for rechargeable lithium-ion batteries. *Energy Environ. Sci.* **2011**, *4*, 2682–2699.
- [2] Poizot, P.; Laruelle, S.; Grugeon, S.; Dupont, L.; Tarascon, J. M. Nano-sized transition-metal oxides as negative-electrode materials for lithium-ion batteries. *Nature* **2000**, *407*, 496–499.
- [3] Wu, Z. S.; Ren, W. C.; Wen, L.; Gao, L. B.; Zhao, J. P.; Chen, Z. P.; Zhou, G. M.; Li, F.; Cheng, H. M. Graphene anchored with Co₃O₄ nanoparticles as anode of lithium ion batteries with enhanced reversible capacity and cyclic performance. *ACS Nano* **2010**, *4*, 3187–3194.
- [4] Qie, L.; Chen, W. M.; Wang, Z. H.; Shao, Q. G.; Li, X.; Yuan, L. X.; Hu, X. L.; Zhang, W. X.; Huang, Y. H. Nitrogen-doped porous carbon nanofiber webs as anodes for lithium ion batteries with a superhigh capacity and rate capability. *Adv. Mater.* **2012**, *24*, 2047–2050.
- [5] Wang, Z. Y.; Zhou, L.; Lou, X. W. Metal oxide hollow nanostructures for lithium-ion batteries. *Adv. Mater.* **2012**, *24*, 1903–1911.
- [6] Zhou, Y. L.; Yan, D.; Xu, H. Y.; Feng, J. K.; Jiang, J. L.; Yue, J.; Yang, J.; Qian, Y. T. Hollow nanospheres of mesoporous Co₉S₈ as a high-capacity and long-life anode for advanced lithium ion batteries. *Nano Energy* **2015**, *12*, 528–537.
- [7] Choi, S. H.; Kang, Y. C. Synthesis for yolk-shell-structured metal sulfide powders with excellent electrochemical performances for lithium-ion batteries. *Small* **2014**, *10*, 474–478.
- [8] Seo, J. W.; Jang, J. T.; Park, S. W.; Kim, C.; Park, B.; Cheon, J. Two-dimensional SnS₂ nanoplates with extraordinary high discharge capacity for lithium ion batteries. *Adv. Mater.* **2008**, *20*, 4269–4273.
- [9] Chen, S. H.; Fan, L.; Xu, L. L.; Liu, Q.; Qin, Y.; Lu, B. 100 K cycles: Core-shell H-FeS@C based lithium-ion battery anode. *Energy Storage Mater.* **2017**, *8*, 20–27.
- [10] Zou, R. J.; Zhang, Z. Y.; Yuen, M. F.; Sun, M. L.; Hu, J. Q.; Lee, C. S.; Zhang, W. J. Three-dimensional-networked NiCo₂S₄ nanosheet array/carbon cloth anodes for high-performance lithium-ion batteries. *NPG Asia Mater.* **2015**, *7*, e195.
- [11] Yu, X. Y.; Yu, L.; Lou, X. W. D. Metal sulfide hollow nanostructures for electrochemical energy storage. *Adv. Energy Mater.* **2016**, *6*, 1501333.
- [12] Kong, D. B.; He, H. Y.; Song, Q.; Wang, B.; Lv, W.; Yang, Q. H.; Zhi, L. J. Rational design of MoS₂@graphene nanocables: Towards high performance electrode materials for lithium ion batteries. *Energy Environ. Sci.* **2014**, *7*, 3320–3325.
- [13] Zhu, C. B.; Mu, X. K.; van Aken, P. A.; Yu, Y.; Maier, J. Single-layered ultrasmall nanoplates of MoS₂ embedded in carbon nanofibers with excellent electrochemical performance for lithium and sodium storage. *Angew. Chem., Int. Ed.* **2014**, *53*, 2152–2156.
- [14] Zhu, C. B.; Kopold, P.; Li, W. L.; van Aken, P. A.; Maier, J.; Yu, Y. A general strategy to fabricate carbon-coated 3D porous interconnected metal sulfides: Case study of Sn/S/C nanocomposite for high-performance lithium and sodium ion batteries. *Adv. Sci.* **2015**, *2*, 1500200.
- [15] Xu, X. D.; Liu, W.; Kim, Y.; Cho, J. Nanostructured transition metal sulfides for lithium ion batteries: Progress and challenges. *Nano Today* **2014**, *9*, 604–630.
- [16] Meduri, P.; Clark, E.; Kim, J. H.; Dayalan, E.; Sumanasekera, G. U.; Sunkara, M. K. MoO_{3-x} nanowire arrays as stable and high-capacity anodes for lithium ion batteries. *Nano Lett.* **2012**, *12*, 1784–1788.
- [17] Lai, C. H.; Huang, K. W.; Cheng, J. H.; Lee, C. Y.; Hwang, B. J.; Chen, L. J. Direct growth of high-rate capability and high capacity copper sulfide nanowire array cathodes for lithium-ion batteries. *J. Mater. Chem.* **2010**, *20*, 6638–6645.
- [18] Feng, C. H.; Zhang, L.; Wang, Z. H.; Song, X. Y.; Sun, K. N.; Wu, F.; Liu, G. Synthesis of copper sulfide nanowire bundles in a mixed solvent as a cathode material for lithium-ion batteries. *J. Power Sources* **2014**, *269*, 550–555.
- [19] Chen, Y. M.; Yu, X. Y.; Li, Z.; Paik, U.; Lou, X. W. D. Hierarchical MoS₂ tubular structures internally wired by carbon nanotubes as a highly stable anode material for lithium-ion batteries. *Adv. Sci.* **2016**, *2*, e1600021.
- [20] An, Q. Y.; Lv, F.; Liu, Q. Q.; Han, C. H.; Zhao, K. N.; Sheng, J. Z.; Wei, Q. L.; Yan, M. Y.; Mai, L. Q. Amorphous vanadium oxide matrixes supporting hierarchical porous Fe₃O₄/graphene nanowires as a high-rate lithium storage anode. *Nano Lett.* **2014**, *14*, 6250–6256.
- [21] Wu, R. B.; Wang, D. P.; Rui, X. H.; Liu, B.; Zhou, K.; Law, A. W. K.; Yan, Q. Y.; Wei, J.; Chen, Z. *In-situ* formation of hollow hybrids composed of cobalt sulfides embedded within porous carbon polyhedra/carbon nanotubes for high-performance lithium-ion batteries. *Adv. Mater.* **2015**, *27*, 3038–3044.
- [22] Liu, Y.; Qiao, Y.; Zhang, W. X.; Li, Z.; Hu, X. L.; Yuan, L. X.; Huang, Y. H. Coral-like α-MnS composites with N-doped carbon as anode materials for high-performance lithium-ion batteries. *J. Mater. Chem.* **2012**, *22*, 24026–24033.

- [23] Gu, Y.; Xu, Y.; Wang, Y. Graphene-wrapped CoS nanoparticles for high-capacity lithium-ion storage. *ACS Appl. Mater. Interfaces* **2013**, *5*, 801–806.
- [24] Zhou, J. W.; Qin, J.; Zhang, X.; Shi, C. S.; Liu, E. Z.; Li, J. J.; Zhao, N. Q.; He, C. N. 2D space-confined synthesis of few-layer MoS₂ anchored on carbon nanosheet for lithium-ion battery anode. *ACS Nano* **2015**, *9*, 3837–3848.
- [25] Zhang, L. S.; Huang, Y. P.; Zhang, Y. F.; Gu, H. H.; Fan, W.; Liu, T. X. Flexible electrospun carbon nanofiber@NiS core/sheath hybrid membranes as binder-free anodes for highly reversible lithium storage. *Adv. Mater. Interfaces* **2016**, *3*, 1500467.
- [26] Fang, W. Y.; Zhao, H. B.; Xie, Y. P.; Fang, J. H.; Xu, J. Q.; Chen, Z. W. Facile hydrothermal synthesis of VS₂/graphene nanocomposites with superior high-rate capability as lithium-ion battery cathodes. *ACS Appl. Mater. Interfaces* **2015**, *7*, 13044–13052.
- [27] Li, H.; Su, Y.; Sun, W. W.; Wang, Y. Carbon nanotubes rooted in porous ternary metal sulfide@N/S-doped carbon dodecahedron: Bimetal-organic-frameworks derivation and electrochemical application for high-capacity and long-life lithium-ion batteries. *Adv. Funct. Mater.* **2016**, *26*, 8345–8353.
- [28] Zhu, C. B.; Wen, Y. R.; van Aken, P. A.; Maier, J.; Yu, Y. High lithium storage performance of FeS nanodots in porous graphitic carbon nanowires. *Adv. Funct. Mater.* **2015**, *25*, 2335–2342.
- [29] Hu, H.; Zhang, J. T.; Guan, B. Y.; Lou, X. W. D. Unusual formation of CoSe@carbon nanoboxes, which have an inhomogeneous shell, for efficient lithium storage. *Angew. Chem., Int. Ed.* **2016**, *55*, 9514–9518.
- [30] Wang, X. F.; Xiang, Q. Y.; Liu, B.; Wang, L. J.; Luo, T.; Chen, D.; Shen, G. Z. TiO₂ modified FeS nanostructures with enhanced electrochemical performance for lithium-ion batteries. *Sci. Rep.* **2013**, *3*, 2007.
- [31] Yang, L. C.; Wang, S. N.; Mao, J. J.; Deng, J. W.; Gao, Q. S.; Tang, Y.; Schmidt, O. G. Hierarchical MoS₂/polyaniline nanowires with excellent electrochemical performance for lithium-ion batteries. *Adv. Mater.* **2013**, *25*, 1180–1184.
- [32] Gao, M. R.; Yao, W. T.; Yao, H. B.; Yu, S. H. Synthesis of unique ultrathin lamellar mesostructured CoSe₂-amine (protonated) nanobelts in a binary solution. *J. Am. Chem. Soc.* **2009**, *131*, 7486–7487.
- [33] Nath, M.; Choudhury, A.; Kundu, A.; Rao, C. N. R. Synthesis and characterization of magnetic iron sulfide nanowires. *Adv. Mater.* **2003**, *15*, 2098–2101.
- [34] Liu, J.; Song, K. P.; Zhu, C. B.; Chen, C. C.; van Aken, P. A.; Maier, J.; Yu, Y. Ge/C nanowires as high-capacity and long-life anode materials for Li-ion batteries. *ACS Nano* **2014**, *8*, 7051–7059.
- [35] Feldmann, C.; Metzmacher, C. Polyol mediated synthesis of nanoscale MS particles (M = Zn, Cd, Hg). *J. Mater. Chem.* **2001**, *11*, 2603–2606.
- [36] Chen, D.; Tang, K. B.; Shen, G. Z.; Sheng, J.; Fang, Z.; Liu, X. M.; Zheng, H. G.; Qian, Y. T. Microwave-assisted synthesis of metal sulfides in ethylene glycol. *Mater. Chem. Phys.* **2003**, *82*, 206–209.
- [37] Xiong, S.; Shen, J.; Xie, Q.; Gao, Y.; Tang, Q.; Qian, Y. T. A precursor-based route to ZnSe nanowire bundles. *Adv. Funct. Mater.* **2005**, *15*, 1787–1792.
- [38] Graf, N.; Yegen, E.; Gross, T.; Lippitz, A.; Weigel, W.; Krakert, S.; Terfort, A.; Unger, W. E. S. XPS and NEXAFS studies of aliphatic and aromatic amine species on functionalized surfaces. *Surf. Sci.* **2009**, *603*, 2849–2860.
- [39] Cho, J. S.; Hong, Y. J.; Kang, Y. C. Design and synthesis of bubble-nanorod-structured Fe₂O₃-carbon nanofibers as advanced anode material for Li-ion batteries. *ACS Nano* **2015**, *9*, 4026–4035.
- [40] Cho, J. S.; Park, J. S.; Kang, Y. C. Porous FeS nanofibers with numerous nanovoids obtained by Kirkendall diffusion effect for use as anode materials for sodium-ion batteries. *Nano Res.* **2017**, *10*, 897–907.
- [41] Wei, X. J.; Tang, C. J.; Wang, X. P.; Zhou, L.; Wei, Q. L.; Yan, M. Y.; Sheng, J. Z.; Hu, P.; Wang, B. L.; Mai, L. Q. Copper silicate hydrate hollow spheres constructed by nanotubes encapsulated in reduced graphene oxide as long-life lithium-ion battery anode. *ACS Appl. Mater. Interfaces* **2015**, *7*, 26572–26578.
- [42] Kim, Y.; Goodenough, J. B. Lithium insertion into transition-metal monosulfides: Tuning the position of the metal 4s band. *J. Phys. Chem. C* **2008**, *112*, 15060–15064.
- [43] Xu, C.; Zeng, Y.; Rui, X. H.; Xiao, N.; Zhu, J. X.; Zhang, W. Y.; Chen, J.; Liu, W. L.; Tan, H. T.; Hng, H. H. et al. Controlled soft-template synthesis of ultrathin C@FeS nanosheets with high-Li-storage performance. *ACS Nano* **2012**, *6*, 4713–4721.
- [44] Fei, L.; Lin, Q. L.; Yuan, B.; Chen, G.; Xie, P.; Li, Y. L.; Xu, Y.; Deng, S. G.; Smirnov, S.; Luo, H. M. Reduced graphene oxide wrapped FeS nanocomposite for lithium-ion battery anode with improved performance. *ACS Appl. Mater. Interfaces* **2013**, *5*, 5330–5335.
- [45] Xing, C. C.; Zhang, D.; Cao, K.; Zhao, S. M.; Wang, X.; Qin, H. Y.; Liu, J. B.; Jiang, Y. Z.; Meng, L. *In situ* growth of FeS microsheet networks with enhanced electrochemical performance for lithium-ion batteries. *J. Mater. Chem. A* **2015**, *3*, 8742–8749.
- [46] Li, L.; Gao, C. T.; Kovalchuk, A.; Peng, Z. W.; Ruan, G. D.; Yang, Y.; Fei, H. L.; Zhong, Q. F.; Li, Y. L.; Tour, J. M.

- Sandwich structured graphene-wrapped FeS-graphene nanoribbons with improved cycling stability for lithium ion batteries. *Nano Res.* **2016**, *9*, 2904–2911.
- [47] Wei, X.; Li, W. H.; Shi, J. A.; Gu, L.; Yu, Y. FeS@C on carbon cloth as flexible electrode for both lithium and sodium storage. *ACS Appl. Mater. Interfaces* **2015**, *7*, 27804–27809.
- [48] Lu, Y. Y.; Zhang, N.; Jiang, S.; Zhang, Y. D.; Zhou, M.; Tao, Z. L.; Archer, L. A.; Chen, J. High-capacity and ultrafast Na-ion storage of a self-supported 3D porous antimony persulfide-graphene foam architecture. *Nano Lett.* **2017**, *17*, 3668–3674.
- [49] Strauss, E.; Golodnitsky, D.; Peled, E. Study of phase changes during 500 full cycles of Li/composite polymer electrolyte/FeS₂ battery. *Electrochim. Acta* **2000**, *45*, 1519–1525.
- [50] Jung, H. G.; Hassoun, J.; Park, J. B.; Sun, Y. K.; Scrosati, B. An improved high-performance lithium-air battery. *Nat. Chem.* **2012**, *4*, 579–585.
- [51] Wei, X. J.; Tang, C. J.; An, Q. Y.; Yan, M. Y.; Wang, X. P.; Hu, P.; Cai, X. Y.; Mai, L. Q. FeSe₂ clusters with excellent cyclability and rate capability for sodium-ion batteries. *Nano Res.* **2017**, *10*, 3202–3211.
- [52] Zhang, F. F.; Wang, C. L.; Huang, G.; Yin, D. M.; Wang, L. M. FeS₂@C nanowires derived from organic-inorganic hybrid nanowires for high-rate and long-life lithium-ion batteries. *J. Power Sources* **2016**, *328*, 56–64.
- [53] Xu, X. J.; Liu, J.; Liu, Z. B.; Shen, J. D.; Hu, R. Z.; Liu, J. W.; Ouyang, L. Z.; Zhang, L.; Zhu, M. Robust pitaya-structured pyrite as high energy density cathode for high-rate lithium batteries. *ACS Nano* **2017**, *11*, 9033–9040.